

A saturated discrete particle model and characteristic-based SPH method in granular materials

Xikui Li^{1,*}, Xihua Chu¹ and D. C. Sheng²

¹*The State Key Laboratory of Structural Analysis for Industrial Equipment, Dalian University of Technology, Dalian 116024, China*

²*School of Engineering, University of Newcastle, Callaghan, NSW 2308, Australia*

SUMMARY

Based on the discrete particle model for solid-phase deformation of granular materials consisting of dry particulate assemblages, a discrete particle–continuum model for modelling the coupled hydro-mechanical behaviour in saturated granular materials is developed. The motion of the interstitial fluid is described by two parallel continuum schemes governed by the averaged incompressible N–S equations and Darcy’s law, respectively, where the latter one can be regarded as a degraded case of the former.

Owing to the merits in both Lagrangian and mesh-free characters, the characteristic-based smoothed particle hydrodynamics (SPH) method is proposed in this paper for modelling pore fluid flows relative to the deformed solid phase that is modelled as packed assemblages of interacting discrete particles. It is assumed that the formulation is Lagrangian with the co-ordinate system transferring with the movement of the solid particles. The assumed continuous fluid field is discretized into a finite set of Lagrangian (material) points with their number equal to that of solid particles situated in the computational domain. An explicit meshless scheme for granular materials with interstitial water is formulated. Numerical results illustrate the capability and performance of the present model in modelling the fluid–solid interaction and deformation in granular materials saturated with water. Copyright © 2007 John Wiley & Sons, Ltd.

Received 23 May 2006; Revised 4 February 2007; Accepted 10 February 2007

KEY WORDS: discrete particle method; smoothed particle hydrodynamics; fluid–solid interaction; characteristic; granular materials

*Correspondence to: Xikui Li, The State Key Laboratory of Structural Analysis for Industrial Equipment, Dalian University of Technology, Dalian 116024, China.

†E-mail: xikuili@dlut.edu.cn, xikuili@hotmail.com

Contract/grant sponsor: National Natural Science Foundation of China; contract/grant numbers: 10672033, 50278012
Contract/grant sponsor: National Key Basic Research and Development Program; contract/grant number: 2002CB412709

Contract/grant sponsor: Australian Research Council

1. INTRODUCTION

Due to its advantages over the continuum mechanics approach in modelling granular flows and capturing the complex micro-mechanical behaviour of granular materials, the discrete element method (DEM) has become an increasing popular approach for studying the behaviour of granular media such as sand and clay, which consist of packed assemblages of interacting discrete particles with voids at the microscopic level, subjected to different types of loading. The DEM [1] is based on modelling of the interaction between individual grains. Significant efforts have been devoted to develop different discrete element models that can describe the normal and tangential contact forces and contact moments in particulate systems [1–14]. As far as granular media saturated by the interstitial liquid is concerned, modelling of pore fluids interacted with solid particles is required.

Existence of interstitial liquid around inter-particles may, in general, be classified into four different states depending on the degree of liquid saturation [15], as shown in Figure 1. They are: (a) pendular state; (b) funicular state; (c) capillary state; and (d) droplet or immersed state. There exist two main types of the mathematical models for modelling interstitial liquid, i.e. the discrete (liquid bridge) [16–19] and continuum [20–25] models. The liquid bridge model is mainly used for low moisture content, i.e. the pendular and funicular state of interstitial liquid, which exists as liquid bridges around the contacts between solid particles and exerts the adhesion and suction effects at liquid–air interfaces. Although the fluid phase in a porous medium is inherently discrete at the microscopic level and the discrete (i.e. the liquid bridge) model takes into account the effect of capillary liquid surrounding the contacts between solid particles on inter-particle adhesion, it is noticed that the discrete models for interstitial liquid are not able to model the fluid transport within a porous medium and can be only used in the case of low liquid content. On the other hand, with an increasing degree of liquid saturation in the medium the capillary and droplet states of interstitial liquid develop and the voids are fully or nearly saturated with liquid. In such cases, the liquid bridge model is no longer valid. To model fluid flow through a porous medium and its interaction with the solid grains of the medium, a continuum model should be employed.

In continuum models, fluid flow through a porous medium is described in terms of macroscopic quantities with no consideration of flow within each individual pore. A representative element volume around any mathematical point in the medium is always assumed to contain porous fluid phase. Macroscopic mass and momentum balance laws suitable for describing the physics of pore fluid are formulated using volume average assumption. Two existing schemes based on Darcy's law and the averaged Navier–Stokes equations, respectively, can be classified into continuum models.

In the scheme based on Darcy's law, the pore fluid–solid particle interaction is described by linearized viscous drags proportional both to the spatial gradients of the pore liquid pressure

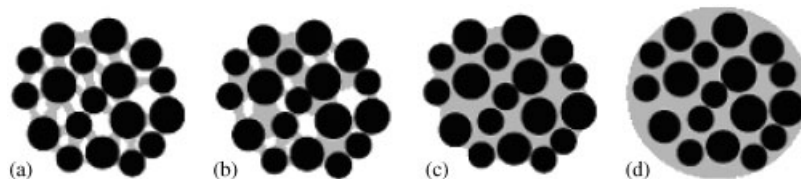


Figure 1. Different states of interstitial water in granular assembly: (a) pendular state; (b) funicular state; (c) capillary state; and (d) droplet state.

and the porosity at local points [26]. In the scheme based on the averaged Navier–Stokes (N–S) equations the solid–fluid interaction force is calculated according to the semi-empirical formulae depending on fluid properties, porosity and relative velocities between the solid and the fluid particles [20–22]. As the pore fluid is assumed inviscid and incompressible, and the dynamic (inertial) effects of the pore fluid flow and the variation of porosity are neglected, the averaged N–S equation scheme may be degraded to the Darcy law scheme, provided the solid–fluid interaction force used in the averaged N–S equation scheme is calculated according to linearized viscous drags used in Darcy law scheme.

The scheme based on Darcy’s law has been widely accepted as the primary one for studying the pore fluid flow interacted with the solid phase in geomechanics, in which the solid phase is modelled a continuum, i.e. the porous continuum at the macroscopic level.

It is accepted that the scheme based on Darcy’s law suits to describe pore fluid flow with low or moderate velocities. In this scheme, all terms related to the fluid acceleration are neglected, and the solid–fluid interaction force calculated according to linearized viscous drag [26] may become inaccurate for high pore fluid velocities.

It was reported [27] that Darcy’s law had been used by several researchers to describe fluid flows through jointed rock media with dense fractures. In these studies, the flow is assumed to be mainly through an interconnected fracture network and the fractures are modelled on the basis of DEM. Until now, to the authors’ knowledge, there have been only a few studies working on the scheme based on Darcy’s law to deal with fluid flow analysis and the interaction of fluid flow with the deformation of the packed assemblage of particles. Among them is the work of Jensen and Preece [28], in which pore fluid flow is governed by the Laplace equation with the primary unknown variable being the fluid pressure potential and numerically simulated by using finite element methods. It implies that the work [28] did not take into account the effect of volumetric strains of the solid skeleton on pore volume change [26], i.e. the coupling effect of the change of collocations of the solid particles, on the mass conservation equation applied to the fluid flow.

The continuum model based on the averaged N–S equations has been widely used for modelling the fluidized beds in chemical engineering and power technology [21, 22, 29], in which the dynamic effects of pore fluid flows and even shear flow effects have to be taken into account owing to the relatively high pore fluid velocities.

The application of the continuum model based on the averaged N–S equations to the simulation of interstitial water flows in saturated granular soils was first owed to the work of Zeghal and Shamy [24, 25] for their attempt to develop a coupled discrete–continuum model. In their work, the DEM was employed to model the assemblages of solid particles, and the fluid–solid particle interactions were quantified using established semi-empirical relationships.

In principle, different numerical methods can be used to analyse the flow through porous media governed by the averaged N–S equations. Zeghal and Shamy [24, 25] used the finite difference method to simulate the flow of interstitial water in granular soils. Owing to the merits in both Lagrangian and mesh-free characters, smoothed particle hydrodynamics (SPH) method is increasingly used in modelling of fluid flow problems. Morris *et al.* [30] and Zhu *et al.* [23] used SPH to simulate fluid flows in porous media modelled as porous continua. Potapov *et al.* [29] presented a computational method that combines SPH and DEM to model flows of solid–liquid mixtures, such as slurries and debris flows, containing a viscous fluid and macroscopic solid particles, in which SPH and DEM are used to simulate fluid flows and solid particles, respectively. The coupling of the solid and fluid phases in the mixtures is achieved by collocating hundreds of SPH fluid particles in the interior of a solid macroscopic particle and satisfying the solid–fluid no-slip

boundary condition at the surface of the solid particle [30]. As a result, the interior SPH fluid points collocated within a solid particle are assumed to move and rotate with the solid particle.

As Lagrangian scheme is used to describe the interaction between solid particles and fluid flow modelled with the discrete elements and the SPH fluid material particles, respectively, we shall assume in the present paper that the formulation is Lagrangian with the co-ordinate systems embedded into each solid particle and transferring with movements of the solid particles. Meantime, the assumed continuous fluid field in the average sense is discretized by means of a finite set of SPH Lagrangian (material) particles with the number equal to the solid particles situated in the computational domain. The centre of each fluid particle is located to overlap with the centre of an associated solid particle at the beginning of a typical time step in an incremental computational procedure. As each fluid particle moves and rotates with the velocities different from those of associated solid particle, a so-called characteristic-based SPH (CBSPH) method is presented to follow fluid material particles and simulate the fluid flow. A discrete–continuum model that combines the DEM model for the solid particulate assemblage and the CBSPH model for the interstitial fluid with two parallel continuum schemes governed by the averaged incompressible N–S equations and Darcy’s law, respectively, is developed in this paper. As compared with the existing models the main features and/or advantages of the proposed model can be stressed as below:

- CBSPH model, derived on the basis of SPH model and possessing the advantages as a meshless Lagrangian computational method, is developed to take into account the movements of fluid particles relative to associated solid particles.
- With regard to the continuum scheme developed to describe interstitial fluid flow governed by Darcy’s law the effect of pore volume change, i.e. the coupling effect of the change of collocations of the solid particles, on the mass conservation equation applied to the fluid flow is taken into account.

Numerical results will illustrate and compare the capability and performance of the two numerical models in modelling the deformation and failure phenomena of the granular materials coupled with interstitial fluid flow.

2. THE DISCRETE ELEMENT METHOD FOR SOLID PARTICLES

The DEM combined with different discrete particle models has become an increasing popular approach for studying the behaviour of granular materials such as sand and clay, which consist of packed assemblages of particles with voids at the microscopic level. In addition, DEM, as a numerical technique, can be used to simulate the flow phenomena of granular materials such as mud avalanches. There exist many different models, among which are the pioneering work of Cundall and Strack [1] and subsequent significant publications [2–13]. The discrete element model used here for solid particles is based on that for dry granular materials presented in [14], which is in turn based on kinematical analysis of relative movements of two typical circular grains with different radii in contact. In the model, both the relative rolling and the relative sliding measurements at contact, including translational and angular velocities (displacements) are defined. Both the rolling and sliding friction tangential forces, and the rolling friction resistance moment, which are constitutively related to corresponding relative motion measurements defined, are formulated and integrated into the framework of the dynamic model of the DEM. The importance of rolling friction

resistance, including both the rolling friction tangential force and the rolling friction resistance moment, was demonstrated [14] in correct simulations of physical behaviour in particulate systems.

For a typical solid particle a , the following Newton's equation of motion in the 2D case are given:

$$m_a \frac{d\mathbf{v}_a}{dt} = \sum_{j=1}^{k_a} \mathbf{f}^{\text{c}j} + \mathbf{f}^{\text{fs}} + m_a \mathbf{g} + \mathbf{f}^{\text{e}} \quad (1)$$

$$I_a \frac{d\omega_a}{dt} = \sum_{j=1}^{k_a} (\mathbf{r}_a^j \times \mathbf{f}^{\text{c}j} + M_{\text{r}}^j) \quad (2)$$

where m_a and I_a are, respectively, the mass and the mass moment of inertia of particle a , \mathbf{v}_a , ω_a stand for, respectively, the translational velocity vector and the angular velocity in the X - Y plane of particle a , k_a is the number of particles in contacts with particle a , $\mathbf{f}^{\text{c}j}$ is the contacting force vector exerted by neighbouring particle j on particle a , \mathbf{f}^{fs} is the fluid-particle interaction force vector acting on the particle a , \mathbf{g} is the gravity acceleration vector, \mathbf{f}^{e} is the other external force vector, \mathbf{r}_a^j is the vector from the centre of the particle a to its contact point with particle j , and M_{r}^j is the rolling friction resistance moment exerted by particle j on particle a .

As the incremental step $I_n = [t_n, t_{n+1}]$ is considered, to calculate M_{r}^j at t_{n+1} , we have first to estimate its predictor $M_{\text{r},tr}^{j,n+1}$ due to the relative rolling angular displacement increment $\Delta\theta_{\text{r}}^j (d\theta_{\text{r}}^j)$, which occurs within the time sub-interval I_n

$$M_{\text{r},tr}^{j,n+1} = M_{\text{rs}}^{j,n+1} + M_{\text{rv}}^{j,n+1} \quad (3)$$

in which

$$M_{\text{rs}}^{j,n+1} = M_{\text{rs}}^{j,n} + \Delta M_{\text{rs}}^j, \quad \Delta M_{\text{rs}}^j = -k_{\theta} \Delta\theta_{\text{r}}^j, \quad M_{\text{rv}}^{j,n+1} = -c_{\theta} \frac{d\theta_{\text{r}}^j}{dt} \quad (4)$$

where k_{θ} and c_{θ} stand for the stiffness coefficient and the coefficient of viscous damping of the rolling friction moment, respectively, $M_{\text{rv}}^{j,n+1}$ reflects the damping effect on rolling friction resistance moment in the model. $M_{\text{r},tr}^{j,n+1}$ has to satisfy Coulomb law of friction and the rolling friction resistance moment is then determined by

$$M_{\text{r}}^j = M_{\text{r},tr}^{j,n+1} \quad \text{if } |M_{\text{r},tr}^{j,n+1}| \leq \mu_{\theta} r |F_{\text{N}}^j| \quad (5)$$

$$M_{\text{r}}^j = \text{sign}(M_{\text{r},tr}^{j,n+1}) \mu_{\theta} r |F_{\text{N}}^j| \quad \text{if } |M_{\text{r},tr}^{j,n+1}| > \mu_{\theta} r |F_{\text{N}}^j| \quad (6)$$

where μ_{θ} and r are the (maximum) static rolling friction moment coefficient and the radius of the particle in consideration, respectively, F_{N}^j is the normal contact force exerted by neighbouring particle j on particle a at t_{n+1} . In the proposed model, the normal contact force is related to the relative normal movement measurement, i.e. the 'overlap' $u_{\text{N}}^{j,n+1}$ at current time instant t_{n+1} and its variation rate with respect to time. $u_{\text{N}}^{j,n+1}$ is defined as the difference between the sum of the radii of the two particles and the distance between the centres of the two particles, i.e.

$$u_{\text{N}}^{j,n+1} = r_a + r_j - \|\mathbf{X}(A_o^{n+1}) - \mathbf{X}(B_o^{j,n+1})\| \quad (7)$$

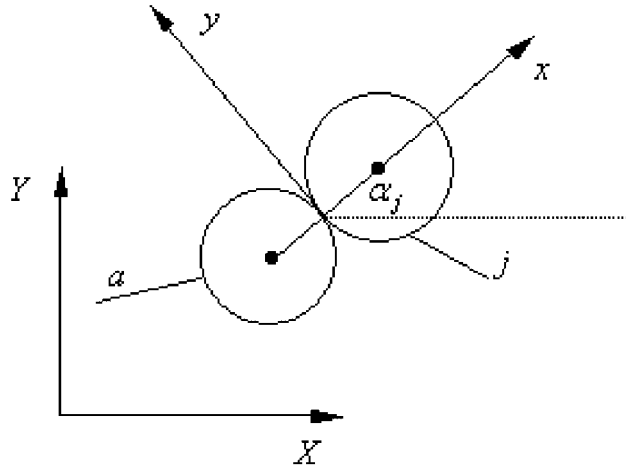


Figure 2. Local co-ordinate system $x-y$ with its origin at the contacting point between particles a and j . α_j is denoted as the inclined angle between the global co-ordinate system \mathbf{X} and the local co-ordinate system \mathbf{x} .

where $r_a, \mathbf{X}(A_o^{n+1}), r_j, \mathbf{X}(B_o^{j,n+1})$ are the radius and the co-ordinates of the centres of particles a and j , respectively. The normal contact force F_N^j between the two particles a and j in contact can be calculated by

$$F_N^j = -k_N u_N^{j,n+1} - c_N \frac{u_N^{j,n+1} - u_N^{j,n}}{\Delta t} \quad \text{if } u_N^{j,n+1} > 0 \tag{8}$$

$$F_N^j = 0 \quad \text{if } u_N^{j,n+1} \leq 0 \tag{9}$$

where k_N and c_N are the compression stiffness coefficient and the coefficient of viscous damping of the normal contact deformation for the granular material.

It is noted that $\mathbf{f}^j = [f_X^j \ f_Y^j]^T$ is the contacting force vector produced by particle j on particle a referred to the global co-ordinate system \mathbf{X} , namely the $X-Y$ plane. Let α_j denote the angle between the X -axis of global co-ordinate system \mathbf{X} to the x -axis of the local co-ordinate system with its origin at the contacting point between particle a and particle j as illustrated in Figure 2, in which the local co-ordinate system is denoted as \mathbf{x} . The contacting force exerted by particle j on particle a in the local co-ordinate system \mathbf{x} is denoted by $\mathbf{F}^{cj} = [F_T^j \ F_N^j]^T$. The transformation between \mathbf{f}^j and \mathbf{F}^{cj} can be expressed in the form

$$\mathbf{f}^j = \mathbf{T}_j^T \mathbf{F}^j, \quad \mathbf{T}_j = \begin{bmatrix} \cos \alpha_j & \sin \alpha_j \\ -\sin \alpha_j & \cos \alpha_j \end{bmatrix} \tag{10}$$

In general, both the sliding and the rolling coexist between two particles in contact. The predictor $F_{T,tr}^{j,n+1}$ of the tangential friction force F_T^j at t_{n+1} due to the relative tangential sliding and rolling

displacement increments $\Delta u_s^j(du_s^j)$ and $\Delta u_r^j(du_r^j)$ can be estimated as

$$F_{T,tr}^{j,n+1} = F_s^j + F_r^j \quad (11)$$

where F_s^j, F_r^j are, respectively, the rolling and the sliding friction tangential forces at t_{n+1} . Hereafter, within this section the subscript $\tau = r, s$ represents in turn the rolling and the sliding friction tangential force, respectively. Then, the predictor $F_{\tau,tr}^{j,n+1}$ of rolling/sliding friction tangent force F_{τ}^j at t_{n+1} due to the relative tangential rolling/sliding displacement increment $\Delta u_{\tau}^j(du_{\tau}^j)$, which occurs within the typical time sub-interval $[t_n, t_{n+1}]$, can be calculated as

$$F_{\tau,tr}^{j,n+1} = f_{\tau}^{j,n+1} + d_{\tau}^{j,n+1} \quad (12)$$

in which

$$f_{\tau}^{j,n+1} = f_{\tau}^{j,n} + \Delta f_{\tau}^j, \quad \Delta f_{\tau}^j = -k_{\tau} \Delta u_{\tau}^j, \quad d_{\tau}^{j,n+1} = -c_{\tau} \frac{du_{\tau}^j}{dt} \quad (13)$$

where k_{τ} and c_{τ} stand for the stiffness coefficient and the coefficient of viscous damping of the rolling/sliding tangential friction, $d_{\tau}^{j,n+1}$ reflects the damping effect on rolling/sliding friction tangent force in the model. $F_{\tau,tr}^{j,n+1}$ has to satisfy Coulomb law of friction and rolling/sliding friction tangential force is determined by

$$F_{\tau}^j = F_{\tau,tr}^{j,n+1} \quad \text{if } |F_{\tau,tr}^{j,n+1}| \leq \mu_{\tau} |F_N^{j,n+1}| \quad (14)$$

$$F_{\tau}^j = \text{sign}(F_{\tau,tr}^{j,n+1}) \mu_{\tau} |F_N^{j,n+1}| \quad \text{if } |F_{\tau,tr}^{j,n+1}| > \mu_{\tau} |F_N^{j,n+1}| \quad (15)$$

where μ_{τ} is the (maximum) static rolling/sliding tangential friction coefficient.

Since $\mu_s \geq \mu_r$ and the predictor $F_{T,tr}^{j,n+1}$ of the tangential friction force F_T^j at t_{n+1} has to satisfy Coulomb law of friction, the tangential friction force is then determined by

$$F_T^j = F_{T,tr}^{j,n+1} \quad \text{if } |F_{T,tr}^{j,n+1}| \leq \mu_s |F_N^j| \quad (16)$$

$$F_T^j = \text{sign}(F_{T,tr}^{j,n+1}) \mu_s |F_N^j| \quad \text{if } |F_{T,tr}^{j,n+1}| > \mu_s |F_N^j| \quad (17)$$

3. INTERSTITIAL FLUID MODELLING—THE TWO CONTINUUM MODELS

3.1. The continuum model based on the averaged N–S equations

The averaged form of the continuity and momentum equations (N–S equations) of the interstitial water modelled as inviscid fluid can be written in terms of averaged variables as

$$\frac{\partial(n\rho_f)}{\partial t} + \frac{\partial(n\rho_f u_i)}{\partial x_i} = 0 \quad (18)$$

$$\frac{\partial(n\rho_f u_i)}{\partial t} + \frac{\partial(n\rho_f u_i u_j)}{\partial x_j} = -n \frac{\partial p}{\partial x_i} + n F_i^{\text{sf}} \quad (19)$$

where ρ_f is the density of interstitial fluid, n the porosity, u_i and p are the fluid averaged (macroscopic) velocity and the pressure of fluid, respectively, F_i^{sf} is the solid–fluid interaction force acting on the fluid, which may be evaluated using [21, 22].

$$\mathbf{F}^{sf} = 150 \frac{(1-n)^2}{n^2} \frac{\mu(\mathbf{v}^n - \mathbf{u}^n)}{d_a^2} + 1.75 \frac{1-n}{n} \rho \frac{(\mathbf{v}^n - \mathbf{u}^n)|\mathbf{v}^n - \mathbf{u}^n|}{d_a} \quad (n \leq 0.8) \quad (20)$$

$$\mathbf{F}^{sf} = \frac{3}{4} C_D \rho \frac{|\mathbf{v}^n - \mathbf{u}^n|(\mathbf{v}^n - \mathbf{u}^n)(1-n)}{d_a} n^{-2.65} \quad (n > 0.8) \quad (21)$$

where \mathbf{v}^n is the velocity of the centre of typical solid particle a at time t_n , \mathbf{u}^n the fluid velocity at the point superposed to the centre of solid particle a at time t_n , d_a the diameter of solid particle a and

$$C_D = \begin{cases} 24(1 + 0.15 Re^{0.687})/Re & (Re < 1000) \\ 0.43 & (Re \geq 1000) \end{cases} \quad (22)$$

$$Re = |\mathbf{v}^n - \mathbf{u}^n| \rho^f n d_a / \mu \quad (23)$$

The fluid–particle interaction \mathbf{f}^{fs} acting on the solid particle can be given according to Newton’s third law of motion, i.e.

$$\mathbf{f}^{fs} = -n \mathbf{F}^{sf} V^p / (1-n) \quad (24)$$

where V^p is the volume of particle a . In combination with the discrete particle model the porosity, which appears above, is defined in principle as

$$n = 1 - \frac{V_s}{V_T} \quad (25a)$$

where V_T is the volume of the representative volume element (RVE) defined with its centre at a particular solid particle, V_s the volume of the solid phase within the RVE; or alternatively defined in principle as

$$n = 1 - \frac{A_s}{A_T} \quad (25b)$$

for the 2D modelling, where A_T is the area of the representative area element (RAE) defined with its centre at a particular solid disc, A_s the area of the solid phase within the RAE. The calculation of the porosity n defined at each discrete solid particle will be further discussed in Section 5.

3.2. The continuum model based on Darcy’s law

The continuum model based on Darcy’s law assumes that average velocities of pore fluid flow relative to the solid phase are determined according to Darcy’s law, i.e.

$$w_i = -k_{ij} \frac{\partial p}{\partial x_j} \quad \text{or} \quad w_i = -k_p \frac{\partial p}{\partial x_i} \quad (26)$$

where w_i is the averaged relative velocities or is termed as Darcy velocities, k_{ij} and k_p are Darcy permeability coefficients for anisotropic and isotropic conditions, respectively, which depend on the viscosity of the granular material, the porosity and the pore geometry. The fluid averaged (macroscopic) velocities u_i of pore fluid can be expressed as

$$u_i = v_i + \frac{w_i}{n} \quad (27)$$

As the fluid–solid interaction is considered the linearized viscous drag force \bar{F}_i^{sf} acting on porous fluid can be, according to Darcy’s law [26], expressed as

$$\bar{F}_i^{\text{sf}} = -k_{ij}^{-1} w_j \quad (28)$$

According to Newton’s third law of motion, the force acting on solid particle a due to the fluid–particle interaction force can be written as

$$f_i^{\text{fs}} = -n \bar{F}_i^{\text{sf}} V^{\text{p}} / (1 - n) = nk_{ij}^{-1} w_j V^{\text{p}} / (1 - n) \quad (29)$$

3.3. The relation between the two continuum models for interstitial fluid flow

As interstitial fluid is assumed as incompressible the averaged N–S continuity and momentum equations (18) and (19) can be reduced to the form

$$\frac{\partial n}{\partial t} + \frac{\partial(nu_i)}{\partial x_i} = 0 \quad (30)$$

$$\frac{\partial(nu_i)}{\partial t} + \frac{\partial(nu_i u_j)}{\partial x_j} = -\frac{n}{\rho_f} \left(\frac{\partial p}{\partial x_i} - F_i^{\text{sf}} \right) \quad (31)$$

Substitution of Equation (30) into Equation (31) with consideration of incompressibility of pore fluid leads to

$$\frac{du_i}{dt} = -\frac{1}{\rho_f} \left(\frac{\partial p}{\partial x_i} - F_i^{\text{sf}} \right) \quad (32)$$

where

$$\frac{du_i}{dt} = \frac{\partial u_i}{\partial t} + \frac{\partial u_i}{\partial x_j} u_j$$

is the Lagrangian or material derivative of u_i with respect to time. If we further assume that (1) the dynamic (inertial) effect of the pore fluid flow is neglected, and (2) the solid–fluid interaction force F_i^{sf} acting on the fluid in Equation (32) is assumed to take the form $F_i^{\text{sf}} = \bar{F}_i^{\text{sf}} = -k_{ij}^{-1} w_j$, instead of Equations (20)–(21), the continuum model based on the averaged N–S equations will degrade to the continuum model based on Darcy’s law.

4. NUMERICAL SCHEMES FOR MODELLING PORE FLUID FLOWS— CHARACTERISTIC-BASED SMOOTHED PARTICLE HYDRODYNAMICS (CBSPH) METHOD

4.1. Smoothed particle hydrodynamics (SPH) method [31]

The basic ideas describing SPH were reviewed by Monaghan [31]. In the present SPH approach the fluid is modelled by a finite set of Lagrangian particles overlapped to the discrete solid particles situated in the computational domain at a particular time level. It is known that a field variable A for a particle at position \mathbf{r}_a denoted by A_a can be approximated by a summation interpolation over the b neighbouring SPH particles

$$A_a(\mathbf{r}_a) = \sum_b A_b \frac{m_b}{\rho_b} W(\mathbf{r}_a - \mathbf{r}_b, h) \quad (33)$$

where m_b , ρ_b , A_b and \mathbf{r}_b are the mass, the density, the value of field variable A and the position vector at particle b denoted by subscript b ; h is the radius of the compact support defined at particle a , W is the smoothing function with the smooth length h , the neighbouring points of particle a are defined by the set $N_a = \{b | \|\mathbf{r}_a - \mathbf{r}_b\| \leq \alpha h\}$, where α is the parameter depending on the particular form of the smoothing function W .

The gradients ∇A_a are computed in terms of the gradients of the smoothing function W by differentiation of Equation (33)

$$\nabla A_a(\mathbf{r}) = \sum_b A_b \frac{m_b}{\rho_b} \nabla W(\mathbf{r} - \mathbf{r}_b, h) \quad (34)$$

As SPH is used to model pore fluid flow in a porous medium consisting of packed assemblage of interacting discrete particles with voids, a CBSPH scheme is proposed in this paper. As mentioned in Section 1 that the assumed continuous fluid field in the average sense is discretized by means of a finite set of Lagrangian (material) points with the number equal to the solid particles situated in the computational domain. The interaction forces between each pair of solid and fluid particles are computed in terms of the relative velocities of both solid and fluid particles. As a typical incremental time step $I_n = [t_n, t_{n+1}]$ with the time step size $\Delta t = t_{n+1} - t_n$ is considered and the time instant t_{n+1} is assumed to be the reference time, we take the solid particles, denoted by the positions of their centres at t_{n+1} , as reference solid particles, meantime, choose fluid material particles at t_{n+1} superposed to reference solid particles as reference fluid particles, which are defined as the nodal points in the SPH discretization for the averaged N–S equations and the mass conservation equation using Darcy's law, respectively. It is noted that to compute Lagrangian derivative of any physical quantity with respect to time for a reference fluid particle along the characteristic in the time interval $I_n = [t_n, t_{n+1}]$, the value of the quantity attributed to the fluid reference particle at time t_n is required. This is one of the key points of the proposed CBSPH scheme as the numerical solution at time t_n does not, in general, directly provide values of the quantity pertaining to reference fluid particles defined at t_{n+1} .

4.2. The formulations of characteristic-based SPH (CBSPH) for the fluid model

We assume that the formulations for the solid phase modelled as packed assemblages of interacting discrete particles are written in the Lagrangian form with local co-ordinate system x – y , for each solid particle, transferring with its movement denoted by solid velocities v_i .

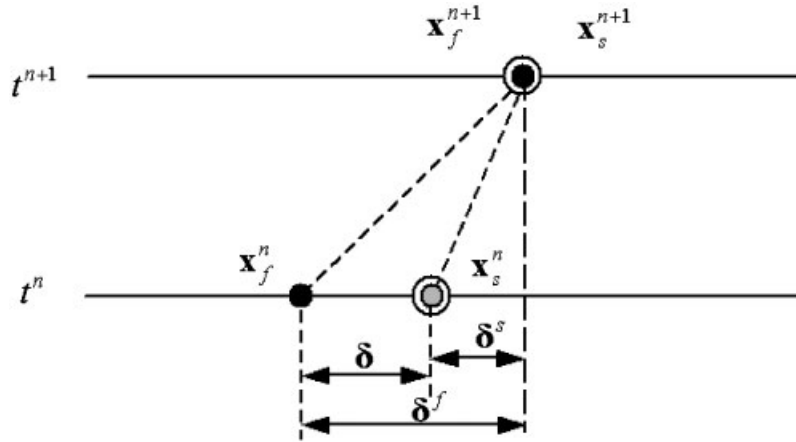


Figure 3. Reference solid and fluid particles overlapped at t^{n+1} and their positions at t^n .

Let us denote by $\mathbf{x}_s^{n+1} : (\mathbf{x}_s(t_{n+1}), t_{n+1})$ the position of the centre of a reference solid particle at time t_{n+1} , while the same reference solid particle had its position $\mathbf{x}_s^n : (\mathbf{x}_s(t_n), t_n)$ at time t_n , as shown in Figure 3, so that $\mathbf{x}_s^{n+1} = \mathbf{x}_s^n + \delta_s + O(\Delta t^2) \cong \mathbf{x}_s^n + \delta_s$ with $\delta_s = \mathbf{v}^n(\mathbf{x}_s^n)\Delta t$ holds.

As the characteristic-based method [32] is employed to describe the pore fluid flow relative to the reference solid particle we define the fluid particle superposed to the reference solid particle at time t_{n+1} as the reference fluid particle, denoted by $\mathbf{x}_f^{n+1} : (\mathbf{x}_f(t_{n+1}), t_{n+1})$ with $\mathbf{x}_f^{n+1} = \mathbf{x}_s^{n+1}$. The same reference fluid particle is located at the position $\mathbf{x}_f^n : (\mathbf{x}_f(t_n), t_n)$ at time t_n so that $\mathbf{x}_f^{n+1} = \mathbf{x}_f^n + \delta_f + O(\Delta t^2) \cong \mathbf{x}_f^n + \delta_f$ with $\delta_f = \mathbf{u}^n(\mathbf{x}_f^n)\Delta t$ holds as shown in Figure 3.

The discretization of the Lagrangian derivative of u_i with respect to time along the characteristic in the time interval $\Delta t = t_{n+1} - t_n$ can be expressed in the form

$$\left. \frac{du_i}{dt} \right|_{\mathbf{x}, t_{n+1}} \cong \frac{1}{\Delta t} [u_i(\mathbf{x}_f^{n+1}, t_{n+1}) - u_i(\mathbf{x}_f^n, t_n)] = \frac{1}{\Delta t} [u_i^{n+1} - u_i(\mathbf{x}_f^n)] \tag{35}$$

It is noted that the numerical solution at time t_n does not, in general, directly provide the value $\mathbf{u}^n(\mathbf{x}_f^n) = \mathbf{u}^n(\mathbf{x}_f^n, t_n)$. Instead, it does provide the value of $\mathbf{u}^n(\mathbf{x}_s^n, t_n)$, i.e. the velocity of the fluid particle, instead of the reference fluid particle, superposed with the reference solid particle at time t_n . To express $\mathbf{u}^n(\mathbf{x}_f^n)$ in terms of $\mathbf{u}^n(\mathbf{x}_s^n)$, we write

$$\mathbf{u}^n(\mathbf{x}_f^n, t_n) = \mathbf{u}^n(\mathbf{x}_s^n - (\delta_f - \delta_s), t_n) = \mathbf{u}^n(\mathbf{x}_s^n - (\mathbf{u}^n(\mathbf{x}_f^n) - \mathbf{v}^n(\mathbf{x}_s^n))\Delta t, t_n) \tag{36}$$

Taylor expansion of Equation (36) in spatial domain at time level t_n can be written as

$$\mathbf{u}^n(\mathbf{x}_f^n) \cong \mathbf{u}^n(\mathbf{x}_s^n) - \Delta t \frac{\partial \mathbf{u}^n(\mathbf{x}_s^n)}{\partial x_i} [u_i^n(\mathbf{x}_f^n) - v_i^n(\mathbf{x}_s^n)] \tag{37}$$

The solution of Equation (37) leads to the expression of $\mathbf{u}^n(\mathbf{x}_f^n)$ in terms of the physical quantities $\mathbf{u}^n(\mathbf{x}_s^n)$, $\partial \mathbf{u}^n(\mathbf{x}_s^n) / \partial x_i$, $\mathbf{v}^n(\mathbf{x}_s^n)$ at the position \mathbf{x}_s^n at time t_n as

$$\mathbf{u}^n(\mathbf{x}_f^n) = \mathbf{B}^{-1} \mathbf{u}^{n*} \quad \text{or} \quad u_i^n(\mathbf{x}_f^n) = B_{ij}^{-1} u_j^{n*} \tag{38}$$

where the components of matrix \mathbf{B} and vector \mathbf{u}^{n*} are expressed by

$$B_{ij} = \delta_{ij} + \frac{\partial u_i^n(\mathbf{x}_s^n)}{\partial x_j} \Delta t \tag{39}$$

$$u_j^{n*} = u_j^n(\mathbf{x}_s^n) + \frac{\partial u_j^n}{\partial x_k} v_k^n(\mathbf{x}_s^n) \Delta t \tag{40}$$

Denote $Q_i = -(1/\rho_f)(\partial p/\partial x_i - F_i^{sf})$ as the external forces applied to the reference fluid particle, the right-hand side terms of Equation (32) is also discretized along the characteristic in the time domain as

$$Q_i \cong \theta Q_i(\mathbf{x}_f^{n+1}, t_{n+1}) + (1 - \theta) Q_i(\mathbf{x}_f^n, t_n) = \theta Q_i^{n+1} + (1 - \theta) Q_i(\mathbf{x}_s^n - \delta + O(\Delta t^2), t_n) \tag{41}$$

with $\theta \in [0, 1]$ and $\delta = \delta_f - \delta_s$. Substitution of the expression for δ

$$\delta = \delta_f - \delta_s = (\mathbf{u}^n(\mathbf{x}_f^n) - \mathbf{v}^n(\mathbf{x}_s^n)) \Delta t \tag{42}$$

into the term $Q_i(\mathbf{x}_f^n, t_n)$ in Equation (41) with the use of Equations (38)–(40) gives

$$\begin{aligned} Q_i(\mathbf{x}_f^n, t_n) &= Q_i(\mathbf{x}_s^n - \delta + O(\Delta t^2), t_n) \cong Q_i(\mathbf{x}_s^n) - \frac{\partial Q_i(\mathbf{x}_s^n)}{\partial x_j} (B_{jk}^{-1} u_k^{n*} - v_j^n) \Delta t \\ &= Q_i^n - \frac{\partial Q_i^n}{\partial x_j} (B_{jk}^{-1} u_k^{n*} - v_j^n) \Delta t \end{aligned} \tag{43}$$

With the use of Equations (35), (38), (41), (43), the temporal discretization of Equation (32) can be written as

$$\frac{1}{\Delta t} [u_i^{n+1} - u_i^n(\mathbf{x}_f^n)] = \theta Q_i(\mathbf{x}_f^{n+1}, t_{n+1}) + (1 - \theta) \left[Q_i^n - \frac{\partial Q_i^n}{\partial x_j} (B_{jk}^{-1} u_k^{n*} - v_j^n) \Delta t \right] \tag{44}$$

i.e.

$$u_i^{n+1} = B_{ij}^{-1} u_j^{n*} + \theta Q_i(\mathbf{x}_f^{n+1}, t_{n+1}) \Delta t + (1 - \theta) \left[Q_i^n - \frac{\partial Q_i^n}{\partial x_j} (B_{jk}^{-1} u_k^{n*} - v_j^n) \Delta t \right] \Delta t \tag{45}$$

It is noted that

$$Q_i(\mathbf{x}_f^{n+1}, t_{n+1}) = -\frac{1}{\rho_f} \left(\frac{\partial p(\mathbf{x}_f^{n+1}, t_{n+1})}{\partial x_i} - F_i^{sf}(\mathbf{x}_f^{n+1}, t_{n+1}) \right)$$

as the second term at the right-hand side of Equation (45) is unknown. With the use of the projection method [33] we compute, at the first step, an intermediate value of the velocities for u_i^{n+1} with the known results at t_n , defined as

$$\tilde{u}_i^{n+1} = B_{ij}^{-1} u_j^{n*} + (1 - \theta) \left[Q_i^n - \frac{\partial Q_i^n}{\partial x_j} (B_{jk}^{-1} u_k^{n*} - v_j^n) \Delta t \right] \Delta t \tag{46}$$

Then, Equation (45) can be re-written in the form

$$u_i^{n+1} = \tilde{u}_i^{n+1} + \theta Q_i(\mathbf{x}_f^{n+1}, t_{n+1}) = \tilde{u}_i^{n+1} - \frac{\theta \Delta t}{\rho_f} \left[\frac{\partial p(\mathbf{x}_f^{n+1}, t_{n+1})}{\partial x_i} - F_i^{\text{sf}}(\mathbf{x}_f^{n+1}, t_{n+1}) \right] \quad (47)$$

As the second step, substitution of Equation (47) into incompressibility condition of the fluid flow

$$\nabla \cdot \mathbf{u}^{n+1} = 0 \quad (48)$$

leads to

$$\nabla^2 p^{n+1} = \nabla \cdot \left(\frac{\rho_f}{\theta \Delta t} \tilde{\mathbf{u}}^{n+1} + \mathbf{F}^{\text{sf}} \right) \quad (49)$$

where $p^{n+1} = p(\mathbf{x}_f^{n+1}, t_{n+1})$, $\mathbf{F}^{\text{sf}} = \mathbf{F}^{\text{sf}}(\mathbf{x}_f^{n+1}, t_{n+1})$. As \mathbf{F}^{sf} is approximately computed from Equations (20) and (21) in terms of the known $\tilde{\mathbf{u}}^{n+1}$, p^{n+1} and \mathbf{u}^{n+1} can be then obtained according to Equations (49) and (47).

To calculate p^{n+1} in the SPH frame, the right-hand side term of Equation (49) for particle a is discretized in the spatial domain in the form

$$Z_a = \nabla \cdot \left(\frac{\rho_f}{\theta \Delta t} \tilde{\mathbf{u}}^{n+1} + \mathbf{F}^{\text{sf}} \right)_a = \frac{\rho_f}{\theta \Delta t} \nabla \cdot (\tilde{\mathbf{u}}^{n+1})_a + \nabla \cdot (\mathbf{F}^{\text{sf}})_a \quad (50)$$

in which

$$\left(\frac{\partial \tilde{u}_i^{n+1}}{\partial x_j} \right)_a = \sum_b (\tilde{u}_{bi}^{n+1} - \tilde{u}_{ai}^{n+1}) \frac{\partial W_a}{\partial x_j} \Delta V_b \quad (51)$$

Here, ΔV_b is used to replace the quantity m_b/ρ_b representing the volume of fluid associated with particle b . The Laplacian of pressure at the left-hand side of the Poisson equation (49) can be, in principle, discretized in the spatial domain in a standard format, however, it is found that the second derivatives of pressure with respect to space are remarkably sensitive to particle disorder. To circumvent this difficulty the Laplacian is formulated as a hybrid of a stand SPH first derivatives with a finite difference approximation of the first derivatives, and the following form based on the formulae given in [30, 34, 35] for the Laplacian is particularly adopted:

$$(\nabla^2 p^{n+1})_a = \sum_b \frac{2\mathbf{r}_{ab} \cdot \nabla W_{ab}}{\mathbf{r}_{ab}^2 + 0.1h^2} p_{ab}^{n+1} \Delta V_b = L_a p_a^{n+1} - L_b \quad (52)$$

where

$$\mathbf{r}_{ab} = \mathbf{r}_a - \mathbf{r}_b, \quad p_{ab}^{n+1} = p_a^{n+1} - p_b^{n+1} \quad (53)$$

$$L_a = \sum_b \frac{2\mathbf{r}_{ab} \cdot \nabla W_{ab}}{\mathbf{r}_{ab}^2 + 0.1h^2} \Delta V_b, \quad L_b = \sum_b \frac{2\mathbf{r}_{ab} \cdot \nabla W_{ab}}{\mathbf{r}_{ab}^2 + 0.1h^2} p_b^{n+1} \Delta V_b \quad (54)$$

Substitution of Equations (52) and (50) into Equation (49) gives

$$L_a p_a^{n+1} = L_b + Z_a \quad (55)$$

It is remarked that as the continuum scheme based on Darcy’s law is adopted to simulate the interstitial fluid flow and Darcy permeability coefficient used for isotropic condition of fluid flow are assumed constant, substitution of Equations (26) and (27) into the mass conservation equation (30) of incompressible flow results in

$$\nabla^2 p = \frac{1}{k_p} \left[\frac{\partial n}{\partial t} + \frac{\partial(nv_i)}{\partial x_i} \right] \tag{56}$$

Let us denote the Laplacian of pressure at particle a at time t_{n+1} as

$$D_a = (\nabla^2 p^{n+1})_a = \frac{1}{k_p} \left[\frac{\partial n}{\partial t} + \frac{\partial(nv_i)}{\partial x_i} \right] \Big|_a^{n+1} \tag{57}$$

It is obtained from Equation (52) that

$$L_a p_a^{n+1} = L_b + D_a \tag{58}$$

An explicit scheme is taken to solve Equations (55) or (58) for p_a^{n+1} at t_{n+1} , in which p_b^{n+1} required to compute L_b is approximately replaced by $p_b(\mathbf{x}_f^n, t_n)$, i.e.

$$\begin{aligned} p_b(\mathbf{x}_f^n, t_n) &= p_b(\mathbf{x}_s^n - \boldsymbol{\delta} + O(\Delta t^2), t_n) \cong p_b(\mathbf{x}_s^n) - \frac{\partial p_b(\mathbf{x}_s^n)}{\partial x_j} (B_{jk}^{-1} u_k^{n*} - v_j^n(\mathbf{x}_s^n))_b \Delta t \\ &= p_b^n - \frac{\partial p_b^n}{\partial x_j} (B_{jk}^{-1} u_k^{n*} - v_j^n)_b \Delta t \end{aligned} \tag{59}$$

where

$$\left(\frac{\partial p}{\partial x_j} \right)_b = \sum_c (p_c - p_b) \frac{\partial W_b}{\partial x_j} \Delta V_c \tag{60}$$

The implementations of the two numerical schemes using CBSPPH method, which are based on the averaged N–S equations and Darcy’s law, respectively, for modelling pore fluid flow can be briefly summarized as below:

1. The procedures based on the averaged N–S equations:
 - (1) With the known values of \mathbf{v}^n , \mathbf{u}^n and the porosity defined at the centre of each local solid particle at time t_n , the solid–fluid interaction force \mathbf{F}^{sf} acting on the fluid and the fluid–particle interaction force \mathbf{f}^{fs} acting on the solid particle are computed by using Equations (21) and (24), respectively.
 - (2) Compute the velocity \mathbf{v}^{n+1} of each solid particle at time t_{n+1} with the known \mathbf{f}^{fs} by using Equation (1) and determine the incremental displacement within the incremental time step $[t_n, t_{n+1}]$.
 - (3) Compute the intermediate velocity $\tilde{\mathbf{u}}^{n+1}$ for each fluid particle with the known \mathbf{F}^{sf} by using Equation (46).
 - (4) With the use of incompressibility condition (48) for the fluid flow solve for p^{n+1} applied to each fluid particle in terms of Equation (55).
 - (5) Determine \mathbf{u}^{n+1} for each fluid particle with known p^{n+1} by using Equation (47).

2. The procedures based on Darcy's law:

- (1) Compute average velocity \mathbf{w}^n of pore fluid flow relative to the solid phase at each fluid particle by using p^n according to Darcy's law (26), then obtain \mathbf{f}^{fs} acting on the solid particle.
- (2) Compute the velocity \mathbf{v}^{n+1} of each solid particle at time t_{n+1} with the known \mathbf{f}^{fs} by using Equation (1).
- (3) Compute the term D_a for each fluid particle in terms of Equation (57).
- (4) Solve for p^{n+1} applied to each fluid particle in terms of Equation (58).

5. NUMERICAL EXAMPLES

In this section, the proposed discrete particle–continuum model, in which solid phase deformation is modelled by the discrete particle model while the motion of the interstitial fluid phase is described by means of the two parallel continuum schemes governed by the averaged incompressible N–S and seepage equations, respectively, is used to simulate coupled hydro-mechanical behaviour in a fluid-saturated panel with $25 \times 44.3 \text{ cm}^2$ rectangular profile. The solid phase of the panel is modelled as a granular assemblage composed by 1249 homogeneous discs with radius of 5 mm, collocated in terms of the hexagonal arrangement as shown in Figure 4. Particularly, the panel of particles is composed of 51 rows of particles, in which 24 or 25 particles are collocated at each odd or even row, respectively.

The material parameters used in the example are chosen as density of solid particle $\rho_s = 2000 \text{ kg m}^{-3}$; $k_n = 6.0 \times 10^8 \text{ N m}^{-1}$, $k_s = 4.0 \times 10^8 \text{ N m}^{-1}$, $k_r = 2.0 \times 10^3 \text{ N m}^{-1}$, $k_\theta = 700 \text{ N m rad}^{-1}$, $\mu_s = 0.5$, $\mu_r = 0.5$, $\mu_\theta r = 1.0 \times 10^{-4} \text{ m}$, $c_n = c_s = c_r = c_\theta = 0$ for discrete particle modelling; water density $\rho_w = 1.0 \times 10^3 \text{ kg m}^{-3}$, hydrodynamic viscosity of pore water $\mu = 1.01 \times 10^{-3} \text{ N m}^{-2} \text{ s}$. To numerically evaluate porosity according to Equation (25b) in the 2D case, the shape and size for a RAE should be specified. In the present work, a circular RAE with the radius $4r$, i.e. four times of the radius of solid particle, centred at a typical interior solid particle a is assumed. For a solid particle located at boundary edges or corners, a RAE with an embowed or sectorial shape can be analogously prescribed. As the sampling value of porosity evaluated according to Equation (25b) at particle a is denoted by

$$n_a^0 = \frac{A^a - A_s^a}{A^a} \quad (61)$$

The porosity at particle a is defined and evaluated according to

$$n_a = \frac{1}{N} \sum_{j=1}^N n_j^0 \quad (62)$$

where N is the total number of solid particles, whose centres lie within the RAE centred at particle a , n_j^0 is evaluated according to Equation (61). For the particulate assemblage formed by a hexagonal arrangement in the present example, initial porosity evaluated at each typical interior solid particle equals to $n = 0.0931$, while initial porosity at each particle located at boundary edges or corners equals to $n = 0.0945$ or 0.1025 , respectively.

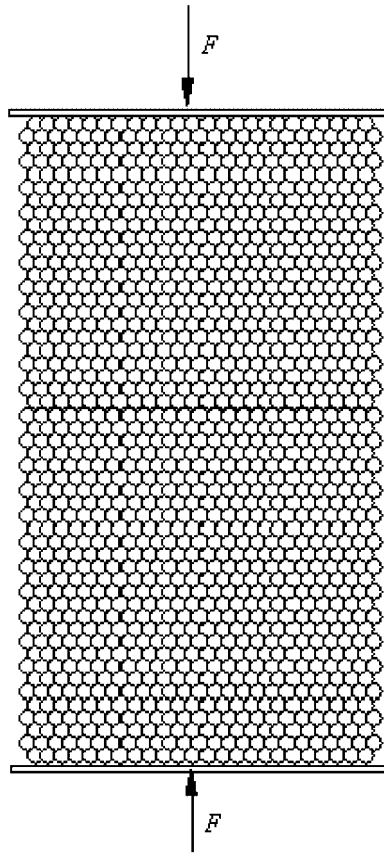


Figure 4. A granular assemblage with $25 \times 44.3 \text{ cm}^2$ rectangular profile generated by 1249 particles with same radius of 5 mm collocated in a regular manner.

The smoothing function, i.e. the kernel function, used in the present CBSPH takes the cubic spline form with smooth length $h = 12.5 \text{ mm}$ given below [31]

$$W(\mathbf{r}, h) = \frac{\sigma}{h^v} \begin{cases} 1 - \frac{3}{2}q^2 + \frac{3}{4}q^3 & \text{if } 0 \leq q \leq 1 \\ \frac{1}{4}(2 - q)^3 & \text{if } 1 \leq q \leq 2 \\ 0 & \text{otherwise} \end{cases} \quad (63)$$

where $q = |\mathbf{r}|/h$, $|\mathbf{r}|$ is the distance between two typical nodal points, v the dimension number and σ a normalization constant with the values $\frac{2}{3}$, $10/7\pi$, $1/\pi$ for $v = 1, 2, 3$, respectively.

The panel with side length of 25 cm is subjected to uniaxial compression between two rigid plates applied by displacement control of the top plate as shown in Figure 4. The plate located on the top boundary of the panel is displaced downwards with constant velocity $6.18 \times 10^{-2} \text{ m s}^{-1}$. The contact of the two plates with the panel is modelled as 'slide sticking', which implies that

vertical displacements of the particles on the bottom and top boundaries of the panel are specified as null and uniformly prescribed values under displacement control, respectively, while the horizontal displacements of the particles on the two boundaries relating to the plates are allowed and governed by frictional resistance law of sliding between the plate and particles with a frictional coefficient equal to 0.5. The particles on the left and right boundaries, except those particles also located on the top and bottom boundaries, are free in both horizontal and vertical directions.

To simulate the pore fluid flow and its coupled effect on the solid particulate assemblage the two different cases distinguished by the boundary conditions prescribed in relation to the pore fluid flow are considered. In the first case (Case I), there are no boundary conditions prescribed for the pore fluid on boundaries of the panel. As the panel is subjected to increasing uniaxial compression drainage (or contrarily imbibition) of pore water is allowed through all boundaries of the panel. Different from the first case in-flow flux of water on the top boundary of the panel is prescribed in the second case (Case II) with constant average velocity $w_y = -1.3 \times 10^{-1} \text{ m s}^{-1}$ relative to the solid-phase movement. The initial uniformly distributed pore water pressure $1.0 \times 10^5 \text{ Pa}$ over whole region of the panel is assumed, except for that at the top boundary in Case II, where $w_y = -1.3 \times 10^{-1} \text{ m s}^{-1}$ is prescribed as the natural boundary condition. One special purpose of the numerical simulation of the panel subjected to Case II is to demonstrate the distinct performances between the two schemes based on the averaged N–S equations and Darcy's law in modelling the flow problems with high velocity of pore fluid and to validate the necessity of developing the scheme based on the averaged N–S equations.

To demonstrate the effect of pore water on the load-carrying capability of the panel and to validate the proposed models in simulating the coupled hydro-mechanical behaviour, the example is executed by using the three different schemes, respectively, which correspond to: (1) saturated discrete particle model using the continuum model based on the averaged N–S equations for modelling interstitial fluid; (2) saturated discrete particle model using the continuum model based on Darcy's law for modelling interstitial fluid; and (3) dry model, i.e. the discrete particle model without consideration of effects of interstitial fluid on the solid phase.

To make sense comparisons of numerical results obtained by the two continuum schemes for simulating the pore fluid flow and coupled hydro-mechanical behaviour, the permeability used for the scheme based on Darcy's law is figured out according to approximate equality of the solid–fluid interaction force acting on the fluid in the two schemes. As averaged porosity used in the example has the value $n \ll 0.8$ we take Equation (20) and re-write it as

$$\mathbf{F}^{\text{sf}} = \mathbf{F}_1^{\text{sf}} + \mathbf{F}_2^{\text{sf}} = -(k_i^{\text{NS}} + k_{nl}^{\text{NS}}) \mathbf{w} \quad (64)$$

where

$$k_i^{\text{NS}} = 150 \frac{(1-n)^2 \mu}{n^3 d_a^2}, \quad k_{nl}^{\text{NS}} = 1.75 \frac{1-n}{n^3} \rho_w \frac{|\mathbf{w}|}{d_a} \quad (65)$$

From the view of Darcy's law, the sum of k_i^{NS} and k_{nl}^{NS} can be regarded as the inverse of equivalent permeability in the scheme based on the averaged N–S equations. k_i^{NS} is constant in the sense of independence from the flow velocity, while k_{nl}^{NS} varies with the absolute value $|\mathbf{w}|$ of Darcy's velocity. With the data $n = 0.0931\text{--}0.1025$, $\mu = 1.01 \times 10^{-3} \text{ N m}^{-2} \text{ s}$, $d_a = 1.0 \times 10^{-2} \text{ m}$, $\rho_w = 1.0 \times 10^3 \text{ kg m}^{-3}$ used in the present example, it can be validated that $k_{nl}^{\text{NS}} \ll k_i^{\text{NS}}$ as $|\mathbf{w}| \ll 150(1-n) \mu / 1.75 \rho_w d_a = 7.85 \times 10^{-1} \text{ cm s}^{-1}$.

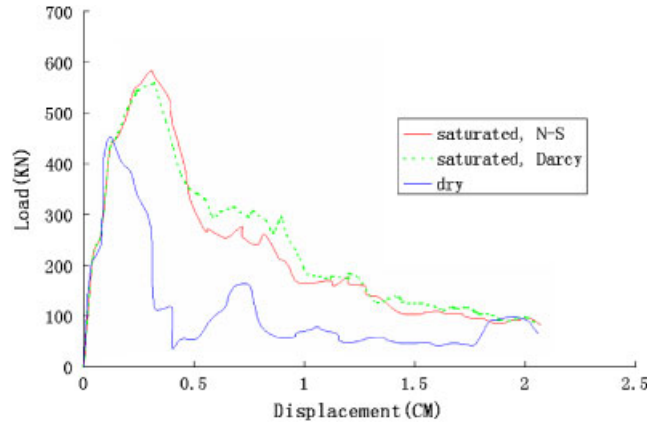


Figure 5. Load–displacement curves for the panel subjected to Case I: uniaxial compression with velocity $6.18 \times 10^{-2} \text{ m s}^{-1}$.

Then, k_{nl}^{NS} can be approximately neglected in determining the permeability used in the scheme based on Darcy’s law, and Darcy permeability is assumed independent from the Darcy velocity and equal to the inverse of k_l^{NS} , i.e.

$$k_p = \frac{1}{k_c^{\text{NS}}} = \frac{n^3 d_a^2}{150(1-n)^2 \mu} \quad (66)$$

which is then taken in the example as $k_x = k_y = 6.5 \times 10^{-7} \text{ m}^4/(\text{N s})$.

It is stressed that enforcement of approximate equality of the solid–fluid interaction force acting on the fluid in the two schemes is only taken as a condition to determine the permeability used in the scheme based on Darcy’s law in terms of material parameters used in the scheme based on the averaged N–S equations, therefore comparisons between the results obtained by using the two schemes make sense, and it does not mean any equivalence of the two schemes based on Darcy’s law and the averaged N–S equations. In reality, porosity n , and therefore the equivalent permeability used to calculate the solid–fluid interaction force in Equation (64), in the scheme based on the averaged N–S equations varies with respect to time and spatial position.

For Case I, load–displacement curves obtained by the three schemes to show the load histories applied on the top of the panel with increasing vertical displacements of the top surface of the panel are given in Figure 5. The results illustrate different performances of the three schemes in reduction of the load-carrying capability, i.e. the softening behaviour, of the panel. It is noted that the water filled up in the pores within the panel plays a role in bearing part of the external loads and enhancing the load-carrying capability of the panel, also in postponing commence of the softening. The higher load-carrying capability estimated by the scheme based on the averaged N–S equations, than that given by the scheme based on Darcy’s law, can be partially attributed to inertial effect of pore fluid flows taken into account in the scheme based on the averaged N–S equations. It can be further observed that there exist three different stages in load histories as shown by the three curves in Figure 5. In the first stage,

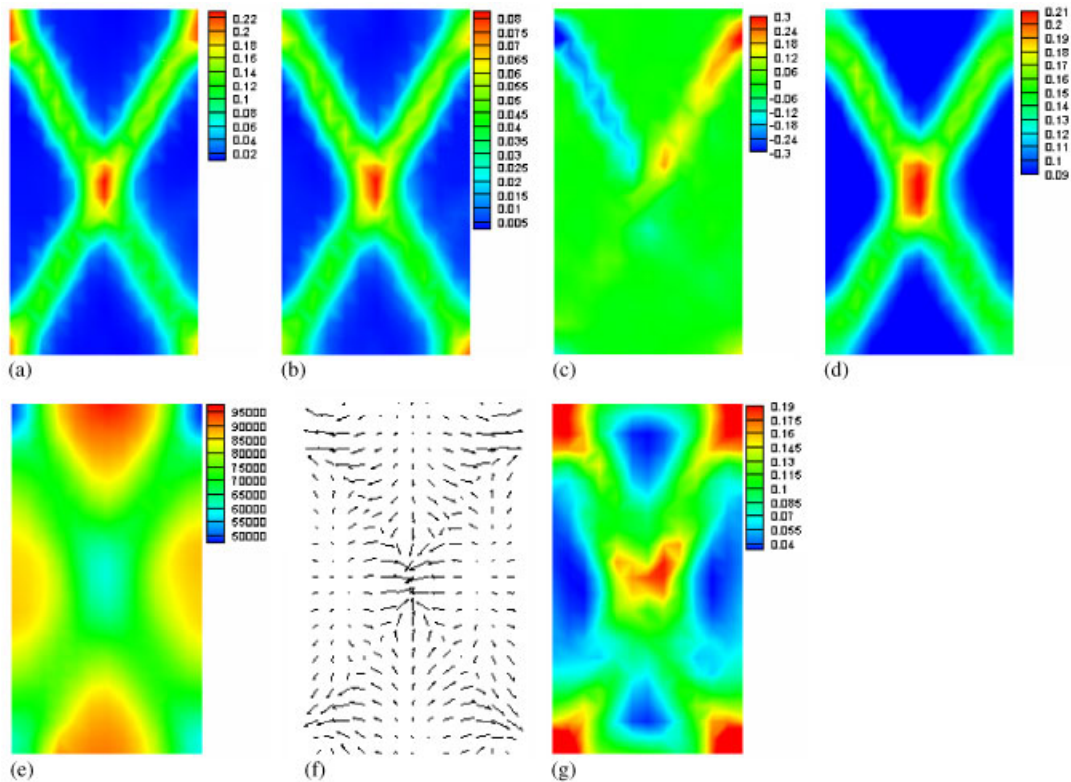


Figure 6. Distributions of physical quantities given by the saturated discrete particle–continuum model based on the averaged N–S equations as the panel is subjected to a uniaxial compression increasing to 1.2 cm: (a) nominal effective strain; (b) nominal volumetric strain; (c) particle rotation; (d) porosity; (e) pore water pressure; (f) streamlines of pore water; and (g) contours of absolute value of averaged pore water velocity relative to solid phase.

the load-carrying capability of the panel increases with increasing displacement until reaching the peak loads of load–displacement curves. It is the second stage after reaching the peak values of the load-carrying capability followed by its constant reductions until it is partially recovered. That is a process of formation of the shear band and gradually losing the load-carrying capability of the panel. Finally, at the third stage, the panel will keep certain amount of residual load-carrying capability generated by sustaining re-locations of the particles in the panel.

Figures 6 and 7 illustrate distributions of nominal effective and volumetric strains, particle rotation, porosity, pore water pressure and streamlines of pore water, contours of absolute value of pore water velocity relative to the solid phase obtained by the two first schemes, i.e. the schemes with consideration of effects of pore fluid flows, respectively, as the panel is subjected to a vertical displacement of 1.2 cm prescribed to the particles at the top boundary of the panel. Here, nominal effective and volumetric strains are computed in terms of the definitions and formulae proposed in [14]. It is observed that nominal effective and volumetric strains, particle rotation and variation

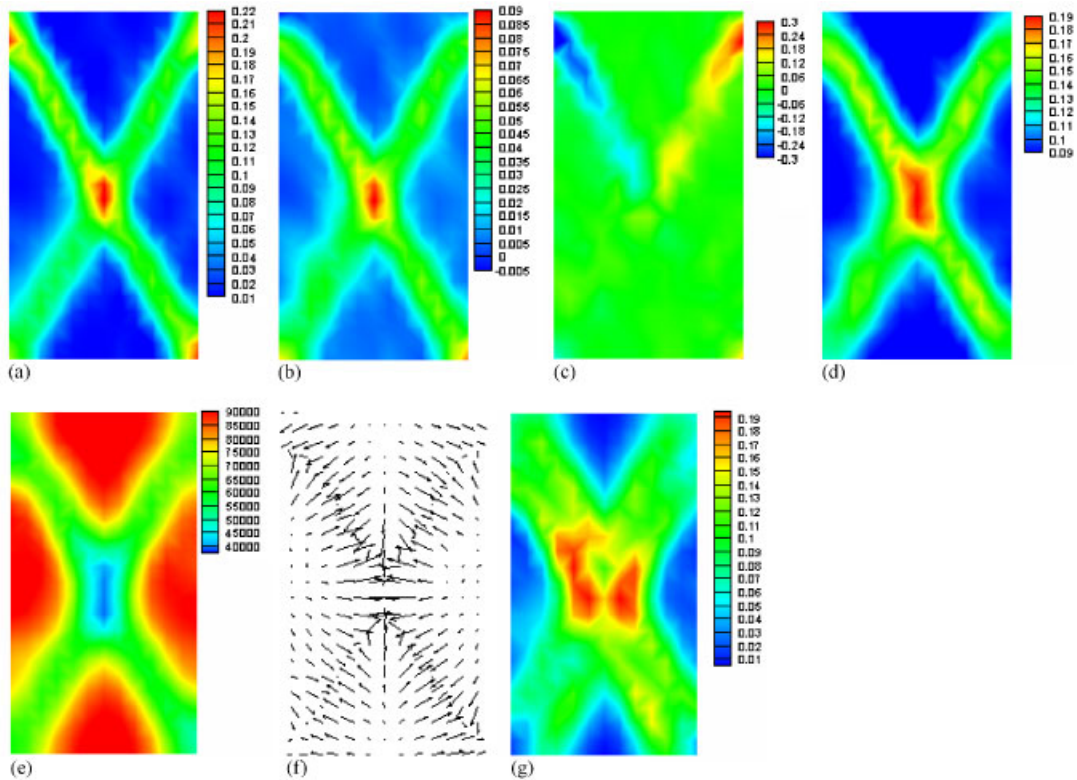


Figure 7. Distributions of physical quantities given by the saturated discrete particle–continuum model based on Darcy’s law as the panel is subjected to a uniaxial compression increasing to 1.2 cm: (a) nominal effective strain; (b) nominal volumetric strain; (c) particle rotation; (d) porosity; (e) pore water pressure; (f) streamlines of pore water; and (g) contours of absolute value of averaged pore water velocity relative to solid phase.

of porosity occur and develop sharply into a narrow band of intense straining characterizing strain localization phenomena, in which evolutions of nominal volumetric strain and porosity present dilatant and swelling characters. The lower values of nominal effective and volumetric strains estimated by the scheme based on the averaged N–S equations as shown in Figures 6(a) and (b) than those given by the scheme based on Darcy’s law shown in Figures 7(a) and (b) can be also attributed to inertial effect of pore fluid flows taken into account in the former scheme. In addition, streamlines of the pore water illustrated in Figures 6(f) and 7(f) prominently demonstrate that pore fluid flows mainly developed within the panel move towards the shear bands, where the porosity increases remarkably.

The load–displacement curves obtained by the three schemes for Case II are illustrated in Figure 8 to show the load histories applied on the top of the panel with increasing vertical displacements prescribed at the top surface and constant in-flow flux of water $w_y = -1.3 \times 10^{-1} \text{ m s}^{-1}$.

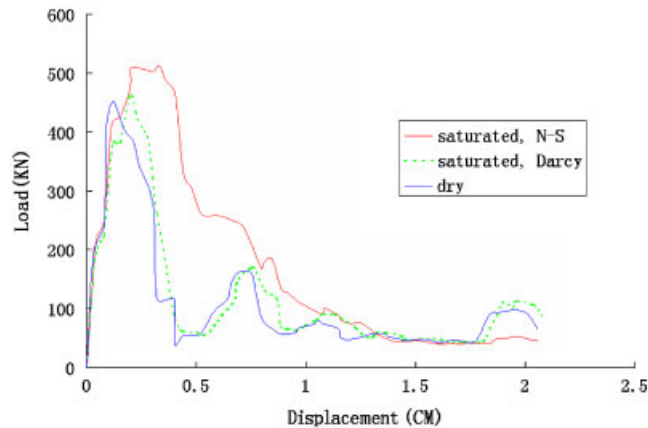


Figure 8. Load–displacement curves for the panel subjected to Case II: uniaxial compression with velocity $6.18 \times 10^{-2} \text{ m s}^{-1}$ combined with in-flow flux of water $w_y = -1 \times 10^{-1} \text{ m s}^{-1}$ applied on the top of the panel.

As analysed from the load–displacement curves given in Figure 5 the pore water plays a role in bearing part of the external loads and therefore enhancing the load-carrying capability. However, the constant in-flow flux of water applied to the top surface of the panel in Case II, which models a rainfall process for instance imposed to geo-structures in practice, will result in deterioration of the load-carrying capability, and therefore, exhibit the effect of the in-flow flux of water, as an environmental load, in impelling the failure process of the panel subjected to the same mechanical load. Indeed, it can be observed in Figure 8 that the load-carrying capabilities predicted by the two schemes based on the averaged N–S equations and Darcy’s law decrease as compared with those, shown in Figure 5, given by the same schemes in Case I.

Figures 9 and 10 illustrate distributions of nominal effective and volumetric strains, particle rotation, porosity, pore water pressure and streamlines of pore water, contours of absolute value of pore water velocity relative to the solid phase obtained by the first two schemes with consideration of effects of pore fluid flows, as the panel is subjected to a vertical compression of 2.1 cm and constant in-flow flux of water $w_y = -1.3 \times 10^{-1} \text{ m s}^{-1}$ prescribed to the top boundary of the panel.

Again, distributions of the state variables such as nominal effective and volumetric strains, particle rotation and porosity shown in Figures 9(a)–(d) and 10(a)–(d) demonstrate the localization character, but are no longer symmetric to the horizontal symmetric axis of the panel due to the in-flow flux of water applied on the top surface of the panel.

Figure 9(e) illustrates that due to the in-flow flux of water input from the top of the panel, the pore water pressure distribution developed over the whole domain of the panel is predicted by the scheme based on the averaged N–S equations, while the pore pressure distribution predicted by the scheme based on Darcy’s law still displays the localization character as shown in Figure 10(e). In addition, the velocities of pore fluid flow relative to the solid phase given by the two schemes based on the averaged N–S equations and Darcy’s law, as shown in Figures 9(f) and (g) and 10(f) and (g), respectively, exhibit notable differences in their directions and absolute

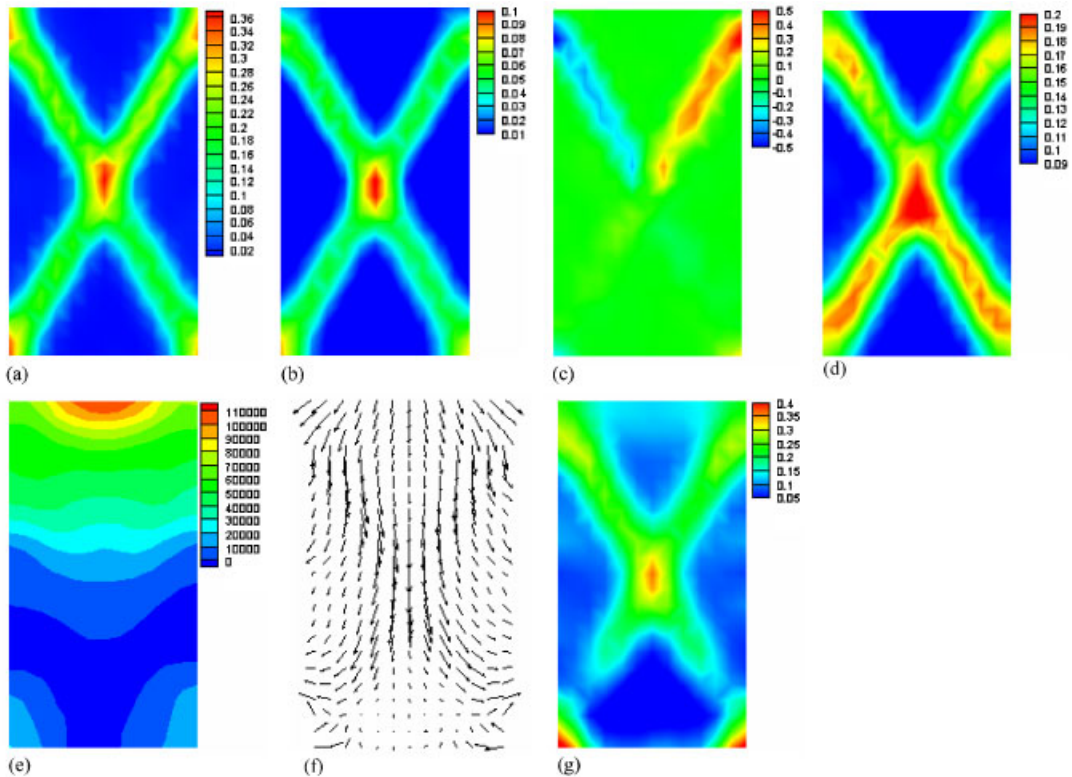


Figure 9. Distributions of physical quantities given by the saturated discrete particle–continuum model based on the averaged N–S equations as the panel is subjected to Case II with a uniaxial compression increasing to 2.1 cm: (a) nominal effective strain; (b) nominal volumetric strain; (c) particle rotation; (d) porosity; (e) pore water pressure; (f) streamlines of pore water; and (g) contours of absolute value of averaged pore water velocity relative to solid phase.

values, which are much larger than the differences between those given in Figures 6(f) and (g) and 7(f) and (g), respectively for Case I.

The differences between the numerical results shown in Figures 9 and 10, particularly in those directly associated with the pore fluid flow, given by the two schemes based on the averaged N–S equations and Darcy’s law, respectively, are much larger than those shown by Figures 6 and 7 that validates the conclusion obtained from experimental studies, i.e. Darcy-based flow model may become inaccurate for high fluid velocities.

Total computing (CPU) times spent to run the example for the whole history of coupled hydro-mechanical process under Case I are 853 and 471 s for the numerical schemes based on the averaged N–S equations and Darcy’s law, respectively, as a P4-2.0 GHz microcomputer with a 512 M memory is used. Hence, the scheme based on Darcy’s law is more efficient in computational efforts required in comparison to the scheme based on the averaged N–S equations and can be successfully used for many applications provided the pore fluid flow is slow.

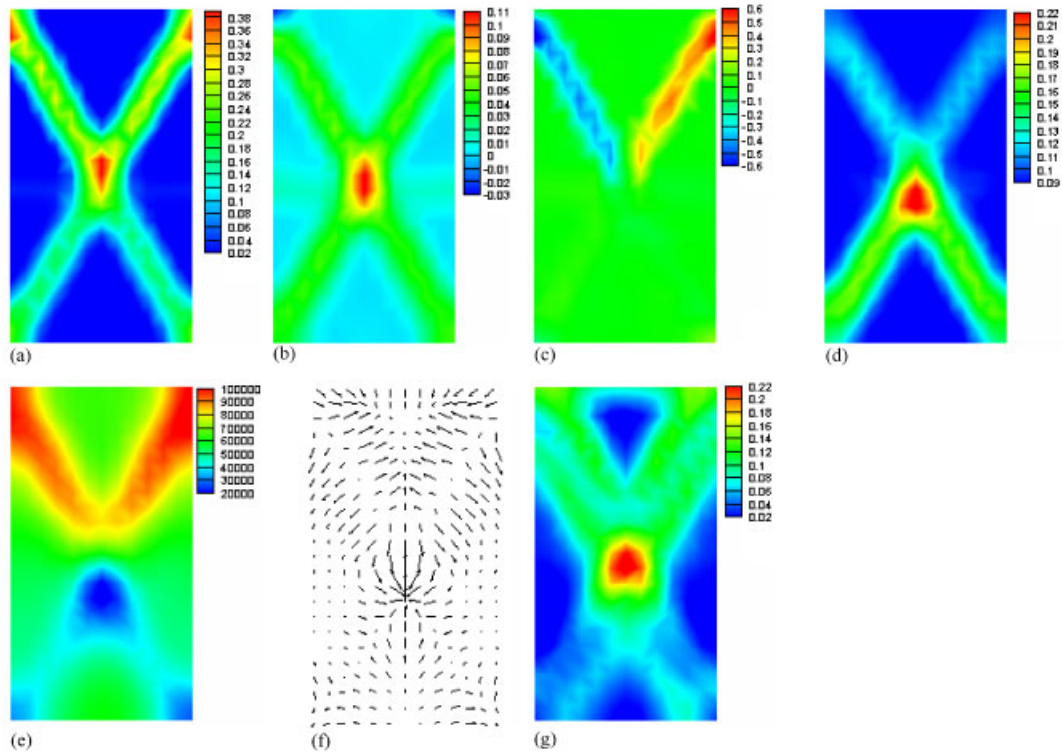


Figure 10. Distributions of physical quantities given by the saturated discrete particle–continuum model based on Darcy’s law as the panel is subjected to Case II with a uniaxial compression increasing to 2.1 cm: (a) nominal effective strain; (b) nominal volumetric strain; (c) particle rotation; (d) porosity; (e) pore water pressure; (f) streamlines of pore water; and (g) contours of absolute value of averaged pore water velocity relative to solid phase.

6. CONCLUDING REMARKS

- (1) Based on the discrete particle model for the dry solid particulate assemblage [14], a coupled discrete particle–continuum model for saturated granular materials is developed. The motion of the interstitial fluid phase and its interaction with the solid phase are described by means of the two parallel continuum schemes governed by the averaged incompressible N–S equations and Darcy’s law, respectively. It is indicated that the latter one can be regarded as a degraded case of the scheme based on the averaged N–S equations.
- (2) In the frame of SPH approach, the characteristic based SPH method is presented for numerical modelling of pore fluid flows relative to the deformed solid phase modelled as packed assemblages of interacting discrete particles with voids. The formulation for pore fluid is Lagrangian with the co-ordinate system transferring with the movement of the solid particles. The assumed continuous fluid field in the average sense is discretized by means of a finite set of Lagrangian (material) points with their number equal to that of the solid particles situated in the computational domain.

- (3) Numerical studies by using the proposed coupled discrete particle–continuum model for saturated granular materials demonstrate the effect of pore fluid flows on the mechanical behaviour of the solid particulate assemblage and the validity of the developed characteristic-based SPH method. It is indicated that the continuum scheme based on Darcy’s law can produce the results close to those given by the scheme based on the averaged N–S equations, provided that the pore fluid is assumed inviscid and incompressible, the dynamic effects of the pore fluid flow and the variation of porosity are insignificant. Hence, the scheme based on Darcy’s law can be successfully used for many applications particularly owing to lower computational efforts required in comparison to the scheme based on the averaged N–S equations. However, the scheme based on Darcy’s law may become inaccurate with increasing pore fluid velocities as demonstrated by the numerical results given in this paper.
- (4) As a micro- and macro-two-scale modelling of saturated granular materials is to be developed, the solid phase of the materials will be modelled by discrete particle assembly and Cosserat continuum in two scales, respectively, while the pore fluid flow in the materials will be modelled by the proposed continuum model based on the averaged incompressible N–S equations (or Darcy’s law) in the micro-scale level and Darcy’s law in the macro-scale level, respectively. The proposed coupled discrete particle–continuum model for saturated granular materials will be a component model in a two-scale discrete–continuum micro-macroscopic approach to saturated granular media.

ACKNOWLEDGEMENTS

The authors are pleased to acknowledge the support of this work by the National Natural Science Foundation of China through contract/grant numbers 10672033, 50278012 and the National Key Basic Research and Development Program (973 Program) through contract number 2002CB412709. The first author is also pleased to acknowledge the support of this work by Australia Research Council through the position of ARC International Fellow offered at University of Newcastle, Australia.

REFERENCES

1. Cundall PA, Strack ODL. A discrete numerical model for granular assemblies. *Geotechnique* 1979; **29**:47–65.
2. Oda M, Konishi J, Nemat-Nasser S. Experimental micromechanical evaluation of strength of granular materials: effects of particular rolling. *Mechanics of Materials* 1982; **1**:269–283.
3. Thornton C. Interparticle sliding in the presence of adhesion. *Journal of Physics D: Applied Physics* 1991; **24**:1942–1946.
4. Elperin T, Golshtein E. Comparison of different models for tangential forces using the particle dynamics method. *Physica A* 1997; **242**:332–340.
5. Iwashita K, Oda M. Rolling resistance at contacts in simulation of shear and development by DEM. *Journal of Engineering Mechanics* 1998; **124**:285–292.
6. Oda M, Iwashita K. *Mechanics of Granular Materials*. Balkema: Rotterdam, 1999.
7. Bardet JP. Observations on the effects of particle rotations on the failure of idealized granular materials. *Mechanics of Materials* 1994; **18**:159–182.
8. Zhang D, Whiten WJ. An efficient calculation method for particle motion in discrete element simulations. *Powder Technology* 1998; **98**:223–230.
9. Zhang D, Whiten WJ. A new calculation method for particle motion in tangential direction in discrete simulations. *Powder Technology* 1999; **102**:235–243.
10. Zhou YC, Wright BD, Yang RY, Xu BH, Yu AB. Rolling friction in the dynamic simulation of sandpile formation. *Physica A* 1999; **269**:536–553.
11. Vu-Quoc L, Zhang X. An elastoplastic contact force–displacement model in the normal direction: displacement-driven version. *Proceedings of the Royal Society of London, Series A* 1999; **455**:4013–4044.

12. Vu-Quoc L, Zhang X, Lesburg L. Normal and tangential force–displacement relations for frictional elasto-plastic contact of spheres. *International Journal of Solids and Structures* 2001; **38**:6455–6489.
13. Feng YT, Han K, Owen DRJ. Some computational issues numerical simulation of particulate systems. *Fifth World Congress on Computational Mechanics*, Vienna, Austria, 2002.
14. Li X, Chu X, Feng YT. A discrete particle model and numerical modeling of the failure modes of granular materials. *Engineering Computations* 2005; **22**(8):894–920.
15. Newitt DM, Conway-Jones JM. A contribution to the theory and practice of granulation. *Transactions of the Institution of Chemical Engineers* 1958; **36**:422–441.
16. Mikami T, Kamiya H, Horio M. Numerical simulation of cohesive powder behavior in a fluidized bed. *Chemical Engineering Science* 1998; **53**(10):1927–1940.
17. Lian G, Thornton C, Adams MJ. A theoretical study of the liquid bridge forces between two rigid spherical bodies. *Journal of Colloid and Interface Science* 1993; **161**:138–147.
18. Liu SH, Sun DA. Simulating the collapse of unsaturated soil by DEM. *International Journal for Numerical and Analytical Methods in Geomechanics* 2002; **26**:633–646.
19. Liu SH, Sun DA, Wang Y. Numerical study of soil collapse behavior by discrete element modeling. *Computers and Geotechnics* 2003; **30**:399–408.
20. Anderson T, Jackson R. A fluid mechanical description of fluidized beds: equation of motion. *Industrial Engineering Chemical Fundamentals* 1967; **6**(4):527–539.
21. Tsuji Y, Kawaguchi T, Tanaka T. Discrete particle simulation of two-dimensional fluidized bed. *Powder Technology* 1993; **77**:79–87.
22. Gera D, Gautam M, Tsuji Y, Kawaguchi T, Tanaka T. Computer simulation of bubbles in large-particle fluidized beds. *Powder Technology* 1998; **98**:38–47.
23. Zhu Y, Morris JP, Fox PJ. A pore-scale numerical model for flow through porous media. *International Journal for Numerical and Analytical Methods in Geomechanics* 1999; **23**:881–904.
24. Shamy UE, Zeghal M. Coupled continuum–discrete model for saturated granular soils. *Journal of Engineering Mechanics* (ASCE) 2005; **131**(4):413–426.
25. Zeghal M, Shamy UE. A continuum–discrete hydromechanical analysis of granular deposit liquefaction. *International Journal for Numerical and Analytical Methods in Geomechanics* 2004; **28**:1361–1383.
26. Zienkiewicz OC, Shiomi T. Dynamic behavior of saturated porous media: the generalized Biot formulation and its numerical solution. *International Journal for Numerical and Analytical Methods in Geomechanics* 1984; **8**(1):71–96.
27. Indraratna B, Ranjith PG, Gale W. Single phase water flow through rock fractures. *Geotechnical and Geological Engineering* 1999; **17**:211–240.
28. Jensen RP, Preece DS. Modeling sand production with Darcy-flow coupled with discrete elements. In *Computer Methods and Advances in Geomechanics*, Desai CS (ed.). Balkema: Rotterdam, 2001; 819–822.
29. Potapov AV, Hunt ML, Campbell CS. Liquid–solid flows using smoothed particle hydrodynamics and the discrete element method. *Powder Technology* 2001; **116**:204–213.
30. Morris JP, Fox PJ, Zhu Y. Modeling low Reynolds number incompressible flows using SPH. *Journal of Computational Physics* 1997; **136**:214–226.
31. Monaghan JJ. Smoothed particle hydrodynamics. *Annual Review of Astronomy and Astrophysics* 1992; **30**:543–574.
32. Zienkiewicz OC, Taylor RL. *The Finite Element Method* (5th edn). Butterworth-Heinemann: Stoneham, MA, 2000.
33. Peyret R, Taylor TD. *Computational Methods for Fluid Flow*. Springer Series in Computational Physics. Springer: New York, Berlin, Heidelberg, 1983.
34. Zhu Y, Fox PJ, Morris JP. Smoothed particle hydrodynamics model for flow through porous media. *Computer Methods and Advances in Geomechanics*, Yuan JX (ed.). Balkema: Rotterdam, 1997; 1041–1046.
35. Shao SD, Lo EYM. Incompressible SPH method for simulating Newtonian and non-Newtonian flows with a free surface. *Advances in Water Resources* 2003; **26**:787–800.